American Mineralogist, Volume 96, pages 23–33, 2011

Crystal chemistry of Th in fluorapatite

YUN LUO,[1,*] JOHN RAKOVAN,[1] YUANZHI TANG,[2] MARIAN LUPULESCU,[3] JOHN M. HUGHES,[4] AND YUANMING PAN[5]

[1]Department of Geology, Miami University, Oxford, Ohio 45056, U.S.A.
[2]School of Engineering and Applied Science, Harvard University, Cambridge, Massachusetts 02138, U.S.A.
[3]Department of Geology, New York State Museum, Madison Avenue, Albany, New York 12230, U.S.A.
[4]Department of Geology, University of Vermont, Burlington, Vermont 05405, U.S.A.
[5]Department of Geological Sciences, University of Saskatchewan, Saskatoon, Saskatchewan S7N 5E2, Canada

ABSTRACT

Through the complementary use of single-crystal X-ray diffraction and X-ray absorption spectroscopy, we present in this paper the first direct results on the site occupancy of thorium in the fluorapatite structure and the structural distortion created by its substitution. Structure refinements based on single-crystal X-ray diffraction data from synthetic Th-doped fluorapatite indicates that Th substitutes almost exclusively in the M2 site. A single-crystal X-ray study of natural fluorapatite from Mineville, New York, also indicated that substituting heavy scatterers (including Th) are concentrated in the apatite M2 site, but definitive site assignments of specific elements were not possible. Extended X-ray absorption fine-structure spectroscopy (EXAFS) was used to probe the local structure of Th in the synthetic fluorapatite (single-crystal form) with a Th concentration of roughly 20000 ppm, as well as Th in the natural Mineville fluorapatite (powder form) with a Th concentration of ~2000 ppm. The EXAFS fitting results also indicate that Th partitions into the M2 site and yield a ~0.05–0.08 Å decrease of average M2-O bond distances associated with local structure distortions that are not obtainable from single-crystal X-ray diffraction studies.

Keywords: Thorium, fluorapatite, single crystal, X-ray diffraction, X-ray absorption spectroscopy, EXAFS

INTRODUCTION

Thorium is found naturally in the Earth's crust with the average concentration of ~10–15 ppm, which is about three times more abundant than uranium and almost as common as lead. At Earth surface conditions, naturally occurring thorium is tetravalent and is dominantly found as ^{232}Th, with half-life of 1.40×10^{10} years. The primary mineral sources of thorium are thorium silicates such as thorite and rare-earth phosphate minerals (e.g., monazite, xenotime, and apatite group minerals). Thorium has extensive industrial applications. For example, it is used in magnesium alloys to provide high strength and creep resistance at elevated temperatures. It is also used as an alloying agent in gas tungsten arc welding to increase the melting temperature of tungsten electrodes (Cary and Helzer 2005). Thorium oxide is used in the preparation of gas mantles because of its high emissivity in the visible spectrum; it also acts as a catalyst in the conversion of ammonia to nitric acid and the production of sulfuric acid (Patnaik 2002). In geology, Th in apatite and monazite is used for dating via the U-Th-Pb and (U, Th)/He geochronometers (Farley and Stockli 2002; Harrison et al. 2002). In the energy industry, thorium has been used in the production of nuclear power and in several compounds in the U^{233} production process. There is increasing interest in the Th fuel cycle due to its natural abundance, attractive physical, chemical and nuclear properties, and reduced plutonium and actinide production (Lung and Gremm 1998). Because of its widespread industrial application, the disposal of thorium waste has become an important environmental concern.

Apatite has the general formula $Ca_5(PO_4)_3X$, where X can be F^- (fluorapatite), Cl^- (chlorapatite), or $(OH)^-$ (hydroxylapatite). The apatite structure is remarkably tolerant of distortion and chemical substitution, and consequently there is a wide range of apatite group minerals (Hughes and Rakovan 2002; Pan and Fleet 2002; Pasero et al. 2010). Because of its common occurrence and its high affinity for many radionuclides (e.g., U, Th, REE, ^{90}Sr, ^{90}Y, etc.), apatite has been used in geochronological and petrogenetic studies for decades (Larsen et al. 1952; Altschuler et al. 1958; Oosthuyzen and Burger 1973). However, little is known about the mechanism of incorporation and structure response of apatite to substituent actinides. Geologically, fluorapatite is by far the most common of the apatite group minerals. It is a ubiquitous accessory phase in igneous, sedimentary, and metamorphic rocks. Because of fluorapatite's high affinity for U, Th, and other radionuclides of environmental concern (Rakovan and Hughes 2000; Rakovan et al. 2002; Pan and Fleet 2002), its low solubility in most surface environments (Elliott 1994), and its resistance to radiation damage (Bros et al. 1996; Weber et al. 1997; Meis et al. 2000; Soulet et al. 2001), there is great interest in fluorapatite to sequester heavy metals and actinides and as a potential solid nuclear waste form (Chen et al. 1997a, 1997b; Carpena and Lacout 1998; Bostick et al. 1999; Ewing and Wang 2002; Carpena et al. 2003; Knox et al. 2003; Wright and Conca

---

* Present address: Department of Earth and Planetary Sciences, Washington University in St. Louis, St. Louis, MO 63130, U.S.A. E-mail: luoy@wustl.edu

0003-004X/11/0001–023$05.00/DOI: 10.2138/am.2011.3438

2004; Conca and Wright 2006; Raicevic et al. 2006; Luo et al. 2009). These uses are directly linked to its chemical composition and structural variation. It is therefore fundamentally important to understand the substitution mechanisms and other intrinsic and external factors that control the chemical composition and structural variation in fluorapatites.

In this study, Th substitution in fluorapatite was examined by the complementary use of diffraction and spectroscopic techniques. The site preference of Th in fluorapatite is examined by single-crystal X-ray diffraction. Extended X-ray absorption fine-structure spectroscopy (EXAFS) is used to obtain quantitative information about the local structure of Th in both natural and synthetic fluorapatite, which includes site preference, near-neighbor distances, and coordination numbers. Thorium has been frequently used as a model for other tetravalent actinides in laboratory studies (Krauskopf 1986; Terra et al. 2006; Trocellier et al. 2006). Thus, understanding the mechanism of incorporation and the structural response of fluorapatite to Th is useful in assessing apatite as a possible host for other tetravalent radionuclides, engineering novel, and better-lasting solid nuclear waste forms and for understanding the behavior of Th in geological systems where fluorapatite is present.

MATERIALS AND METHODS

Samples used in this study include both natural fluorapatite from Mineville, New York, and synthetic single crystals of Th-doped fluorapatite. Details of synthesis methods and crystal characterization of the synthetic single-crystal sample can be found in Luo et al. (2009).

Mineville fluorapatite

The Mineville deposit is a low-Ti, Fe (oxide)-P-REE ore. It is, in part, similar to Kiruna-type iron deposits based on its mineralogical and chemical composition (McLelland et al. 1988; Foose and McLelland 1995; Lupulescu 2003; Lupulescu and Pyle 2006). Minerals in the main ore of the Mineville iron deposit are dominantly magnetite and apatite with minor to trace amounts of hematite (martite < 1%), stillwellite-(Ce), allanite-(Ce), monazite-(Ce), edenite, actinolite, ferro-actinolite, scapolite, titanite, and zircon. Minor micrometer-size inclusions of allanite-(Ce), parisite, and monazite-(Ce) are found in some apatite crystals.

The apatite used in this study was separated from a sample (Fig. 1a) from the so-called "Old Bed" in the Mineville deposit (McKeown and Klemic 1954). This ore body contains magnetite and apatite in variable ratios with trace hedenbergite and quartz. Fluorapatite is characterized by high concentrations of REE, Th, and U. It appears as red, brown or yellow, 1 to 5 mm, hexagonal prisms embedded in magnetite (Fig. 1b). The red and/or brown color is due to inclusions of hematite along the fractures or within the crystal. McKeown and Klemic (1954) described a 0.05 mm rim of a reddish-brown aggregate of monazite, bastnäsite, and hematite on some of the apatite crystals from the Old Bed. The apatite used for this study did not show inclusions other than hematite and magnetite in polished thin sections or in BSE images.

Major elements in apatite from the Mineville deposit were determined by electron microprobe. The analyses of the crystals (Table 1) were performed on a JEOL 733 superprobe at the Electron Microprobe Laboratory, Rensselaer Polytechnic Institute, Troy, New York. Standards used for analyses were: apatite (Ca, P), jadeite (Na), tephroite (Si), synthetic fayalite (Fe), thorite (Th), topaz (F), sodalite (Cl), strontianite (Sr), synthetic $LaPO_4$ (La), synthetic $CePO_4$ (Ce), synthetic $NdPO_4$ (Nd), and synthetic YPO_4 (Y) at 15 keV and 50 nA operating conditions. The data were reduced using a ZAF correction routine. The concentrations of trace elements (Table 2) were determined by ICP-MS with a PerkinElmer/Sciex Elan 6100 DRC in the Department of Geology at Union College, Schenectady, New York. Single apatite crystals of several different colors (dark red, light red, and yellow red) were handpicked under the binocular microscope and dissolved in 5% HNO_3 at room temperature. No obvious residual solids were found after dissolution.

Single-crystal XRD

Both the natural Mineville sample and the synthetic sample measurements were made at room temperature with a Bruker Platform goniometer equipped with an APEX 4K CCD detector and Mo*K*α radiation, for a full sphere of data comprising 4500 frames collected at a detector distance of 5.04 cm, with 0.2° frame width. The measured intensities were corrected for Lorentz and polarization effects using the program SAINT and an empirical absorption correction was applied using the

FIGURE 1. Fluorapatite and magnetite from the "Old Bed" Mineville, New York. (**a**) The rock sample from which the fluorapatite crystals were taken. (**b**) Close up of sample in **a** showing a ~3 mm long red brown crystal of fluorapatite, which has elongate hexagonal morphology.

TABLE 1. Chemical composition and empirical formula of natural fluorapatite from Mineville, New York, from electron microprobe analyses (JOEL 733)

No.	P_2O_5 (wt%)	SiO_2	CaO	ThO_2	Y_2O_3	FeO	Na_2O	La_2O_3	Nd_2O_3	Ce_2O_3	F	Cl	O=F, Cl	Total
1	35.0	2.73	48.6	0.15	1.40	0.00	0.15	1.32	1.21	2.70	4.04	0.06		97.3
2	35.0	2.67	49.1	0.20	1.51	0.00	0.14	1.35	1.34	2.84	4.83	0.08		99.0
3	35.0	2.78	49.0	0.25	1.59	0.02	0.14	1.24	1.33	2.67	4.23	0.08		98.5
4	34.0	2.77	47.1	0.22	1.48	3.04	0.12	1.26	1.24	2.66	4.08	0.07		98.0
Avg.	34.8	2.74	48.5	0.21	1.50	0.77	0.14	1.29	1.28	2.71	4.30	0.07		98.2

Note: Average empirical formula: $(Ca_{9.45}Th_{0.01}Fe_{0.12}Na_{0.05}Y_{0.15}La_{0.09}Nd_{0.08}Ce_{0.18})_{\Sigma 10.13}(P_{5.36}Si_{0.50})_{\Sigma 5.86}O_{24}F_{2.48}Cl_{0.02}$. The standard deviations for P, Si, Ca, Th, Y, Fe, Na, La, Nd, Ce, F, Cl are 0.24, 0.09, 0.46, 0.06, 0.05, 0.03, 0.03, 0.10, 0.09, 0.12, 0.12, 0.02, respectively.

TABLE 2. Trace elements concentrations (ppm) in natural fluorapatite from Mineville, New York, determined by ICP-MS with a PerkinElmer/Sciex Elan 6100 DRC

Sample	Color	Sr (ppm)	Y	La	Ce	Pr	Nd	Sm	Eu	Gd	Tb	Dy	Ho	Er	Tm	Yb	Lu	Pb	Th	U
R1	light red	124	7966	7077	14105	1784	8029	1388	139	1452	203	1250	319	814	121	680	87	176	765	216
R2	dark red	157	11825	10510	20797	2645	11904	2048	203	2128	295	1821	465	1178	177	1000	127	79	1645	318
Y3	yellow red	139	10544	9382	18511	2335	10445	1830	181	1897	264	1626	414	1057	157	890	114	93	1262	275
Avg.		140	10112	8990	17804	2255	10126	1755	174	1825	254	1566	399	1016	151	857	109	116	1224	270

Note: The average standard deviation for REEs is approximately 1%.

program SADABS (Bruker 1997). The structures were routinely refined from the apatite starting model (Hughes et al. 1991) in space group $P6_3/m$ using the Bruker SHELXTL version 6.10 package of programs, with neutral-atom scattering factors and terms for anomalous dispersion. Refinements were performed with anisotropic thermal parameters for all atoms, and the structures were refined on F^2.

The results of the structure refinement of the synthetic sample were reported in Luo et al. (2009). For the Mineville sample, the crystal data are reported in Table 3; the atomic positions, site occupancy factors, and equivalent anisotropic displacement parameters are reported in Table 4; and selected bond lengths are reported in Table 5.

EXAFS DATA COLLECTION AND ANALYSIS

Powder EXAFS on Mineville fluorapatite

Thorium L_3-edge EXAFS measurements on the Mineville fluorapatite were conducted at the beamline X18B of the National Synchrotron Light Source, Brookhaven National Laboratory. Single crystals were handpicked from the Mineville specimen and ground into powder form, then loaded in an acrylic frame holder and sealed on both ends by two layers of Kapton tape. The SEM analysis, including backscattered electron imaging and EDS, of this powdered Mineville sample shows there are no other Th-bearing phases. The X-ray storage ring was operated at 2.8 GeV with a maximum current of 280 mA. A pair of Si (111) channel cut crystals, with one crystal detuned by 20% to reduce harmonics, was used as monochromator to select the desired X-ray energy. The monochromator was calibrated by assigning the first inflection point of the L_3-absorption edge of Th in a ThO_2 model compound to 16300 eV. The X-ray beam size was collimated to 7 mm (horizontal) by 0.5 mm (vertical). All spectra were collected at room temperature in fluorescence mode at 90° to the incident beam using a Canberra 13-element Ge solid-state detector. Each EXAFS scan was collected within 30 min by scanning the monochromator energy from 16200 to 16270 eV with 5 eV steps, and from 30 eV below the absorption edge (16300 eV) to 30 eV above with 0.5 eV steps, using 2 s signal recording time. From 30 eV above the absorption edge, 0.05 $Å^{-1}$ steps in photoelectron wave number with 5 s signal recording time were used. Thirty-three scans were collected at room temperature and averaged to obtain the raw spectrum for EXAFS fitting.

TABLE 3. Single-crystal XRD experimental details and crystal data for Mineville fluorapatite

Space group	$P6_3/m$
a (Å)	9.4023(2)
c (Å)	6.8955(2)
V (Å^3)	527.92(2)
Scan time	15 s
Effective transmission	0.912517–1.000
R_{int} (–)	
before SADABS absorption correction	0.0232
after SADABS absorption correction	0.0171
Measured reflections	8886
Unique reflections	546
Refined parameters	43
$R1$, $F_o > 4\sigma(F_o)$ data	0.0181
$R1$, all unique data	0.0181
$wR2$	0.0398
Largest difference peaks (e$^-$ Å^{-3})	+0.40, –0.37
Goodness-of-Fit	1.216

Micro-EXAFS on synthetic single-crystal fluorapatite

Because of the small volume of the synthesized fluorapatite, single-crystal micro-EXAFS experiments were performed. Single crystals of Th-doped fluorapatite were screened by SEM using backscattered imaging and EDS analysis to avoid intergrown phases. Because specimens for EXAFS study are conventionally in powder form, the EXAFS signal that results from the interferences of photoelectron scattering is averaged over all directions in the crystal structure, and there is no polarization dependence. However, this situation is different for micro-EXAFS on single-crystal specimens. Synchrotron radiation exhibits 100% polarization with the electronic vector parallel to the horizontal orbital plane. When micro-EXAFS is performed on a single crystal, depending on the local environment of the absorbing atom, the EXAFS spectrum will be different for different orientations of the crystal. To interpret polarized micro-EXAFS data, it is necessary to know the crystallographic orientation of the sample with respect to the polarization direction of X-ray beam during data collection. To do this, we have designed and built a portable goniometer that duplicates the geometry of our laboratory Bruker APEX diffractometer goniometer (Fig. 2). Crystal orientation is determined by X-ray diffraction at our home institution. The portable goniometer is then set up on the experimental table at synchrotron facilities and the crystal can

TABLE 4. Atomic positions, equivalent anisotropic thermal parameter, and site occupancy factor for atoms in Mineville fluorapatite

Atom	*x*	*y*	*z*	U_{eq}	*sof*
Ca1	2/3	1/3	0.0009(1)	0.0137(2)	1.051(5)
Ca2	0.7598(1)	0.7518(1)	1/4	0.0132 (2)	1.115(5)
P	0.3696(1)	0.3986(1)	1/4	0.0091(2)	0.964(5)
O1	0.8414(2)	0.5155(2)	1/4	0.0162(4)	1
O2	0.4672(2)	0.5884(2)	1/4	0.0192(4)	1
O3	0.6580(2)	0.9150(2)	0.0703(2)	0.0227(3)	1
F	0	0	1/4	0.0346(8)	1

TABLE 5. Selected bond lengths in Mineville fluorapatite determined by single-crystal XRD

Ca1-O1 (×3)	2.402(1)	Ca2-O1	2.689(2)
Ca1-O2 (×3)	2.459(1)	Ca2-O2	2.388(2)
Ca1-O3 (×3)	2.808(1)	Ca2-O3 (×2)	2.354(1)
Mean	2.556	Ca2-O3 (×2)	2.506(1)
		F	2.297(1)
		Mean	2.442
P-O1	1.541(2)		
P-O2	1.545 (2)		
P-O3 (×2)	1.541(1)		
Mean	1.542		

be positioned in any specific, known orientation for EXAFS data collection (Fig. 2).

Thorium L_3-edge micro-EXAFS measurements were conducted at beamlines X27A and sector 13BM of the National Synchrotron Light Source, Brookhaven National Laboratory, and Advanced Photon Source, Argonne National Laboratory, U.S.A., respectively. The data from X27A were better suited for analysis and are thus presented here. For beamline X27A, the X-ray storage ring was operated at 2.8 GeV with a maximum current of 280 mA. A monochromator with a pair of water-cooled channel cut Si (111) crystals was used to select the desired X-ray energy. The X-ray beam was focused to about 10 μm vertically and 15 μm horizontally by a focusing system that consists of two 20 cm long, dynamically bent rhodium-coated silicon mirrors arranged in Kirkpatrick-Baez (KB) geometry. The measurements were made in fluorescence mode using a Canberra 13-element germanium array solid-state X-ray detector with digital signal processing (DSP) technology. Each EXAFS scan was collected within 80 min by scanning the monochromator energy from 16 200 to 16 270 eV with 5 eV steps, and from 30 eV below the absorption edge (16 300 eV) to 30 eV above with 0.7 eV steps. From 30 eV above the absorption edge, 1 eV steps from 16 330 to 16 630 eV, and 2 eV steps from 16 630 to 17 300 eV were used. At each energy point the signal was recorded for 5 s. Sixteen scans were collected at room temperature and averaged to obtain the raw spectrum for EXAFS fitting.

Model compound

ThO_2 was used as a model compound for EXAFS analysis of both Mineville and synthetic fluorapatite. ThO_2 was mixed with BN for a Th concentration of 1 wt% and sealed in a lucite sample holder covered with Kapton tape. The EXAFS scans were collected in fluorescence mode at beamline X27A using the same scan parameters as the synthetic fluorapatite described above. Eleven scans were collected at room temperature and averaged to obtain the raw spectrum for EXAFS fitting.

EXAFS data analysis

Data processing and analysis were performed using the programs WinXAS (Ressler 1997) and IFEFFIT (Newville 2001). Theoretical phases and backscattering amplitudes were calculated using FEFF7 (Ankudinov and Rehr 1997). Individual scans were averaged after energy calibration and careful alignment to improve the signal-to-noise ratio. Background subtraction and normalization used a linear pre-edge function and a second-order post-edge polynomial. The χ function was extracted using

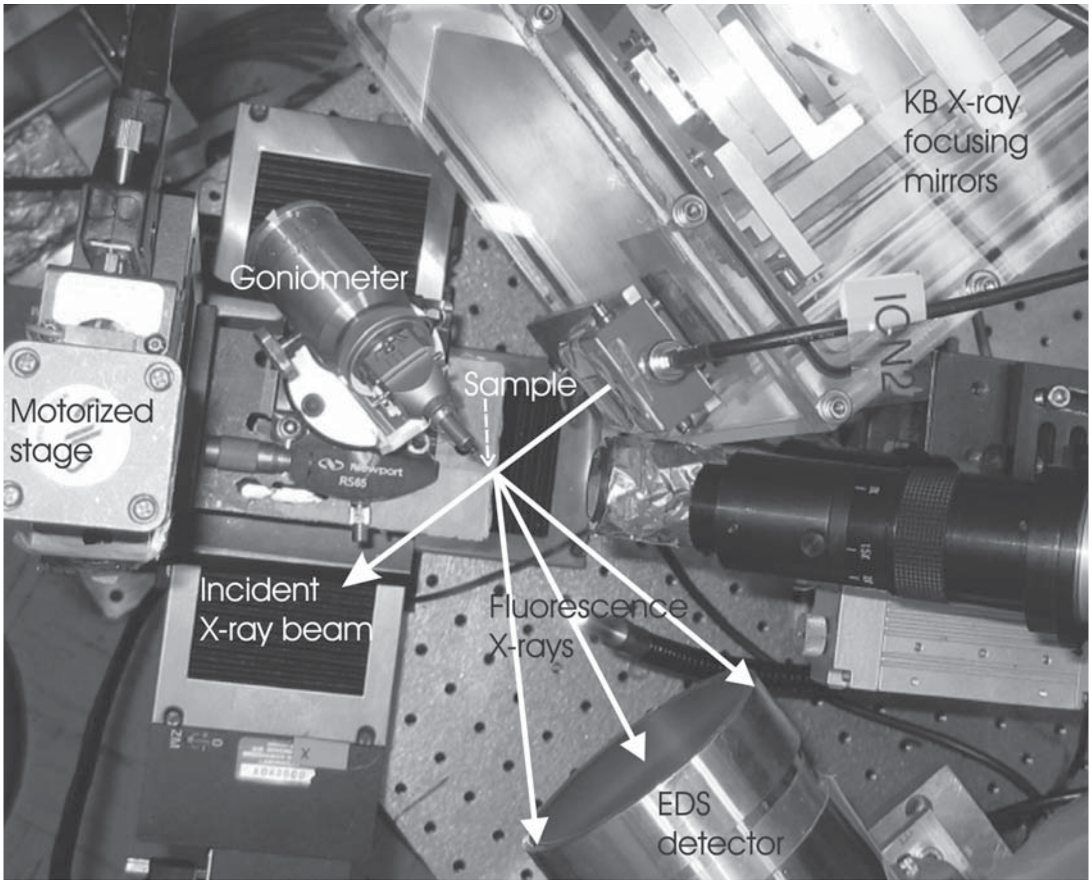

FIGURE 2. Micro-XAS experimental setup at synchrotron facility showing the portable goniomter. The single-crystal sample was mounted on the end of a glass fiber and fixed to the portable goniometer as indicated by the dashed arrow. The paths of incident X-ray beam and fluorescence X-ray are showed by solid arrows.

a cubic spline with k^3 weighting. All shell-by-shell fitting was done in R-space using the Fourier transforms of the k^3-weighted $\chi(k)$ functions. A single threshold energy value (E_0) was allowed to vary during fitting. The amplitude reduction factor (S_0^2) determined from fits of the ThO_2 model compound was found to equal 1, and S_0^2 for both Mineville and synthetic fluorapatite was fixed at a value of 1. Because of the large correlation between coordination number (CN) and Debye-Waller (DW) factor, CN values for fluorapatite were allowed to vary for the first shell (Ca-O) and were fixed for higher shells.

As discussed in the next section (Table 6), first-nearest-neighbor interatomic distances around each of the two M sites vary in the apatite structure. According to Kelly et al. (2008), the spatial resolution of the Fourier transform of EXAFS data are $\Delta R = \pi/2\Delta k$. The Th L_3-edge EXAFS data collected have a usable k-range of ~1.5 to 10 Å^{-1}, which results in a resolution in R of ~0.20 Å. This resolution is not enough to differentiate all distinct first shell interatomic distances around the absorbing Th atom in the samples. Consequently, atoms of the same nature that are <0.20 Å apart were fit using one path in our fitting process. The EXAFS fitting results of the interatomic distances of each shell, Table 7, are thus averaged distances of all atoms within the same shell.

The goodness-of-fit in EXAFS modeling is evaluated by the relative percentage of residual, which is the deviation between the experimental spectra and fitted spectra, defined as

$$\text{Residual (\%)} = \frac{\sum_{i=1}^{N}\left|y_{\text{exp}}(i) - y_{\text{theo}}(i)\right|}{\sum_{i=1}^{N}\left|y_{\text{exp}}(i)\right|} \times 100$$

with N the number of data points in the fit window, y_{exp} and y_{theo} the experimental and theoretical data points, respectively (Ressler 1997). Errors for the fitting parameters are estimated from fits of the model compounds. Error estimates are ±0.01 Å for the R value of the first oxygen shell, and ±0.05 Å for larger distance shells. For coordination number, which is correlated to the Debye-Waller factor, the error is estimated at ±15% for the first oxygen shell and ±35% for shells at larger distance. Estimated errors for the Debye-Waller factors are ±0.001 Å^2 for the first-shell and ±0.005 Å^2 for higher order shells.

RESULTS

The structural formula for the apatite unit cell can be written as $^{[IX]}M1_4{}^{[VII]}M2_6(TO_4)_6X_2$. For fluorapatite (FAP), M = Ca, T = P, and X = F. There are two structural sites in FAP into which Th could possibly substitute, the M1 and M2 sites (Fig. 3). These two sites have distinctly different local coordination environments. Table 6 gives the backscattering paths calculated by FEFF for M1 and M2 sites in both pure natural FAP using the structure model of Hughes et al. (1989) and synthetic Th-doped FAP (Luo et al. 2009). According to the calculation for pure FAP, the M1 site, occupied by Ca, is coordinated to nine O atoms at ~2.399–2.807 Å, and the shells of greater distance consist of three P at ~3.207 Å, two Ca at ~3.425–3.453 Å, three P at ~3.585 Å and six Ca

TABLE 7. Fitting parameters of natural, synthetic fluorapatite samples, and ThO_2

Shell	CN	R (Å)	σ² (Å²)	E_0 (ev)	R (%)
ThO_2 (Standard)					
Th-O	8 fixed	2.39	0.007	4.86	13.8
Th-Th	12 fixed	3.94	0.004		
Th-O	24 fixed	4.60	0.007		
Th-Th	6 fixed	5.57	0.006		
$Ca_5(PO_4)_3F$ (Natural Th-bearing fluoraptite in powder form)					
Th-O	6.98	2.39	0.009	4.33	11.57
Th-P	2 fixed	3.18	0.004		
Th-P	1 fixed	3.40	0.002		
Th-P	2 fixed	3.64	0.012		
Th-Ca	10 fixed	4.14	0.03		
$Ca_5(PO_4)_3F$ (Synthetic Th-doped fluorapatite single crystal fitted without P*)					
Th-O	6.76	2.36	0.007	4.68	2.94
Th-P	2 fixed	3.17	0.007		
Th-P	1 fixed	3.52	0.008		
Th-P	2 fixed	3.72	0.003		
Th-Ca	5.05 correlated*	4.02	0.016		
Th-Ca	4.95 correlated*	4.10	0.008		
$Ca_5(PO_4)_3F$ (Synthetic Th-doped fluorapatite single crystal fitted with P*)					
Th-O	7.16	2.38	0.007	5.25	5.96
Th-P	2 fixed	3.22	0.004		
Th-P	1 fixed	3.52	0.006		
Th-P	2 fixed	3.73	0.002		
Th-Ca	4.99 correlated†	3.78	0.03		
Th-Ca	5.01 correlated†	4.14	0.004		

Notes: Error estimates are ±0.01 Å for R value of the first oxygen shell, and ±0.05 Å for higher distance shells. For CNs, the error is estimated at ±15% for the first oxygen shell and ±35% for shells at higher distance. Estimated errors for the Debye-Waller factors are ±0.001 Å^2 for the first shell and ±0.005 Å^2 for higher shells

* P stands for polarization correction.

† Th-Ca paths were correlated to be add to 10 for synthetic Th-doped FAP.

TABLE 6. Coordination environment of M1 and M2 sites in natural fluorapatite and Th-doped synthetic fluorapatite single crystal

M1 site					M2 site				
Shell	CN	Amp.*	R in natural FAP†	R in Th-doped FAP‡	Shell	CN	Amp.	R in natural FAP†	R in Th-doped FAP‡
M1-O1	3	100.00	2.399	2.396	M2-F	1	100.00	2.311	2.288
M1-O2	3	93.55	2.457	2.454	M2-O3	2	100.00	2.348	2.350
M1-O3	3	63.14	2.807	2.806	M2-O2	1	48.05	2.374	2.383
M1-P	3	50.04	3.207	3.205	M2-O3	2	84.37	2.501	2.494
M1-Ca1	1	14.86	3.425	3.427	M2-O1	1	34.10	2.700	2.683
M1-Ca1	1	14.48	3.453	3.456	M2-P	1	27.63	3.075	3.071
M1-P	3	35.61	3.585	3.576	M2-P	1	23.08	3.265	3.246
M1-Ca2	3	28.45	3.961	3.961	M2-P	1	17.91	3.494	3.504
M1-Ca2	3	26.46	4.045	4.051	M2-P	2	30.16	3.680	3.686
					M2-Ca1	2	26.41	3.961	3.961
					M2-Ca2	2	26.36	4.003	3.963
					M2-Ca1	2	24.57	4.045	4.051
					M2-Ca2	4	46.05	4.143	4.133

* Amp. is an approximate amplitude that FEFF calculates for each path relative to that of the first path. It is indicative of the paths' contribution to the EXAFS spectrum.

† Calculated based on structure of natural FAP from Hughes et al. (1989).

‡ Calculated based on structure of FAP from Luo et al. (2009).

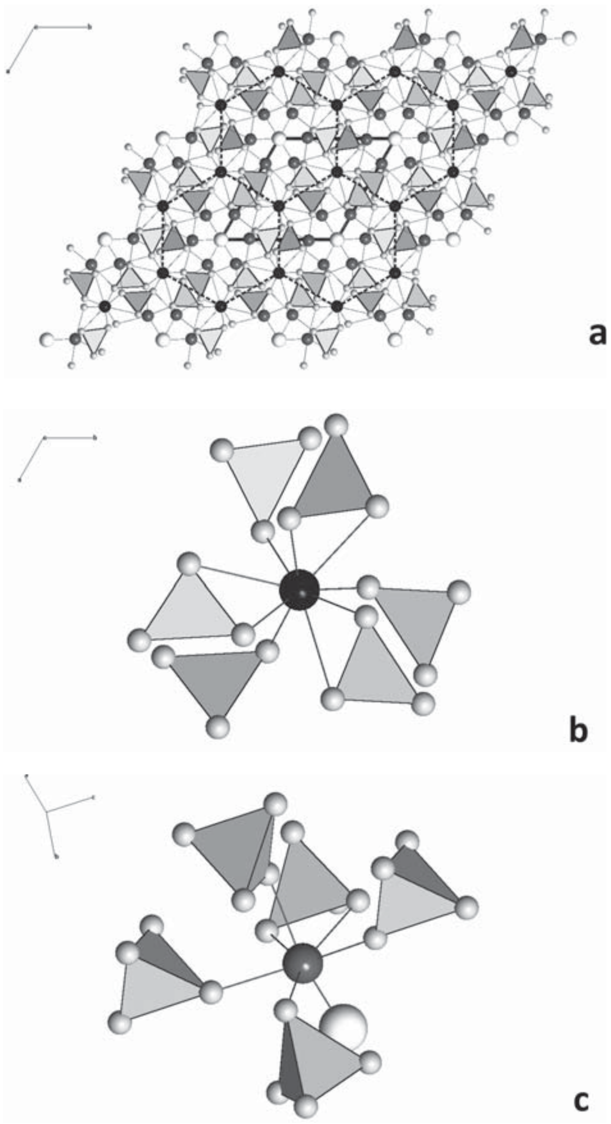

FIGURE 3. (**a**) Overall structure of fluorapatite showing the M1-PO_4 frame and F anion channel, dark black sphere represents M1 site and dark gray sphere represents M2 site. (**b**) Nearest neighbor environment of the M1 site. (**c**) Nearest neighbor environment of the M2 site. Both **b** and **c** emphasize the second nearest neighbor (PO_4 tetrahedra).

at ~3.961–4.045 Å. The M2 site, also occupied by Ca, is seven-coordinated with six O atoms and one column anion (F in this case). The first shell of the M2 site consists of one F at ~2.311 Å and six O atoms at ~2.348–2.700 Å, and longer distance shells are one P at 3.075 Å, one P at 3.265 Å, one P at 3.494 Å, two P at 3.680 Å, six Ca at ~3.961–4.045 Å, and four Ca at ~4.143 Å. Because EXAFS cannot distinguish between O and F due to their similar scattering properties, the first shell of M2 site was fitted using seven O atoms instead of six O atoms and one F atom. From crystal structure refinement (Luo et al. 2009) of the synthetic Th-doped FAP, the M1 site is coordinated to nine O atoms at ~2.396–2.806 Å, and the higher distance shells consist of three P at ~3.2105 Å, two Ca at ~3.427–3.456 Å, three P at ~3.576 Å and six Ca at ~3.961–4.051 Å. The first shell of M2 site consists of one F at ~2.288 Å and six O atoms at ~2.350–2.683 Å, and the higher distance shells are one P at 3.071 Å, one P at 3.246 Å, one P at 3.504 Å, two P at 3.686 Å, six Ca at ~3.961–4.051 Å, and four Ca at ~4.133 Å. As discussed below, structure models of the natural FAP from Hughes et al. (1989) and the synthetic Th-doped FAP from Luo et al. (2009) were used as starting models for EXAFS fitting of Th in Mineville FAP and Th in synthetic FAP, respectively.

Thorium in Mineville fluorapatite

Thorium in the Mineville apatite was examined using single-crystal X-ray diffraction and powder EXAFS. The results of the single-crystal study are permissive of the Th residing in the apatite M2 site, as was found in the previously cited single-crystal study using synthetic Th-doped apatite (Luo et al. 2009). Table 1 gives the chemistry for Mineville apatite, and illustrates the large amounts of heavy scatterers found in it. Table 4 illustrates the site occupancy factors for the M1 and M2 sites in Mineville apatite, and illustrates that the M2 site incorporates a larger proportion of those scatterers, as the M1 contains 21.0(1) electrons, whereas the M2 site contains 22.3(1) electrons. The large variety of heavy atoms and the small amount of Th relative to those other atoms prohibits definitive site assignments as was possible in the synthetic phase, but the single-crystal study illustrates that the M2 site incorporates a larger portion of the heavy scatterers as has been found in previous studies (Luo et al. 2009; Hughes et al. 1991).

Because the Mineville FAP was prepared as a powder for EXAFS data collection, the EXAFS signal that results from photoelectron scattering and interference is averaged over all crystallographic directions, and thus, there is no polarization dependence. For analysis of the EXAFS data from this sample, backscattering paths calculated using initial models of M1 and M2 sites from pure Th free natural FAP (Hughes et al. 1989) were adopted as the starting models. The raw and fitted k^3-weighted χ functions for the Th-bearing Mineville FAP are shown in Figure 4a. The corresponding radial structure functions (RSFs), obtained by Fourier-transformation of the χ functions, are shown in Figure 4b. The data and fit ranges, along with the goodness-of-fit parameters for this fit are shown in Table 8. All scattering paths used and parameters determined in the fit are listed in Table 7.

Fits were performed using the initial parameters calculated for each of the two M sites, and fixing the coordination numbers of higher shells. Regardless of the starting model, the first coordination shell is always best fit with 6.98 ± 0.04 O atoms at ~2.39 Å, indicating that Th substitutes into M2 site. This is consistent with our single-crystal results described below. Figure 4b shows that the second RSF peak is at R + ΔR ~3.1–3.2 Å. This shell is best fitted by two P atoms at ~3.18 Å. There is a split of the third shell in the RSFs spectrum. The best-fit model suggests that the first peak of the split third shell that is at R + ΔR ~3.5–3.7 Å is due to one P atom at 3.40 Å and two P atoms at 3.64 Å and the second split peak of the third shell that is at R + ΔR ~4.1–4.2 Å is best fitted by ten Ca atoms at a distance of 4.14 Å. The large Debye Waller factor of 0.03 for the second peak in the split shell, suggests a large distribution of Th-Ca distances that cannot be individually resolved. According to the crystallographic model, the coordination number of the first shell, the overall distribution of calculated paths that contribute to the second and the split third shells indicate that the coordination environment of Th in the Mineville FAP sample is similar to M2 site, with two P atoms at 3.180 ± 0.001 Å (equal to the average of one P atom at 3.075 Å and one P atom at 3.265 Å), one P atom at 3.403 ± 0.002 Å, two P atoms at 3.642 ± 0.002 Å, and ten Ca atoms at 4.149 ± 0.002 Å. The same fitting approach using the M1 site model failed because of the two M1-M1 (Th-Ca in this case) paths at the distance of ~3.42–3.45 Å in the model (Table 6) do not fit the experimental data.

Although powder X-ray diffraction, chemical, and SEM analysis of the powdered Mineville FAP sample indicate that there are no other Th phases present, we tested two other structure models including thorite ($ThSiO_4$) and thorianite (ThO_2) to further exclude possible Th-bearing phases. In the thorite structure Th is coordinated by eight O atoms (four equatorial O atoms at ~2.36 Å and four axial O atoms at ~2.46 Å) in the first shell of nearest neighbor atoms. The second shell is composed of two Si atoms at ~3.16 Å that share the axial O atoms with Th along the edges of the Si tetrahedron. At a distance of ~3.9 Å, there are four Th atoms together with four Si atoms that contribute to the third shell around Th. Similar to Th in the fluorapatite M1 and M2 site models, the fitting results of the first shell using the thorite model is ~7 O atoms at ~2.39 Å. The best fit for the second shell is two Si atoms at ~3.19 Å. However, the attempt to model the third shell using the thorite structural model was not successful because of the inability to model the splitting of the third shell. The results of the coordination number of the first shell together with the failure to model the third shell excluded the possibility of Th in mineral thorite. The thorianite structure is relatively simple with Th coordinated with 8 O atoms as the first shell at a distance of ~2.43 Å, and 12 Th atoms as the second shell at ~3.96 Å. Any attempt to introduce the second Th-Th backscattering path in the fit failed, suggesting that Th signal collected is not from thorianite.

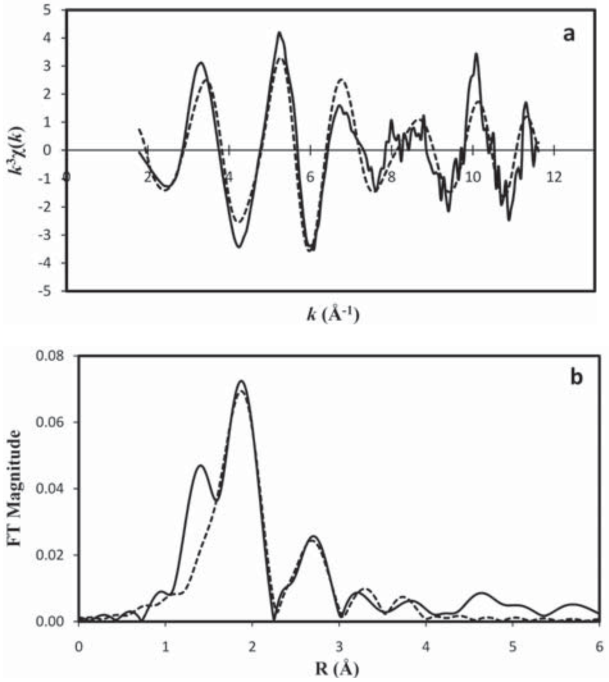

FIGURE 4. EXAFS data and best fits for Mineville fluorapatite. (**a**) the k^3 weighted EXAFS data (solid line) and best fit (dotted line). (**b**) corresponding Fourier transform amplitudes (solid line) and best fit in R-space (dotted line).

Thorium in synthetic single-crystal fluorapatite

In the single-crystal XRD study by Luo et al. (2009), it was found that Th substituted almost exclusively into the M2 site in FAP. The crystal with ~2 wt% Th, which is ~50 × 100 μm in size, was studied by micro-EXAFS. The sample was mounted on a glass fiber and fixed to a goniometer head. An orientation matrix of this sample was collected on a Bruker APEX diffractometer, from which the polarization vector of the synchrotron beam was calculated (Luo et al. manuscript in prep). In short, the orientation matrix was used to calculate the crystallographic direction that is perpendicular to the X-ray beam direction and in the horizontal plane when the omega, two theta, and phi goniometer angles of Bruker APEX diffractometer are set at zero. The portable goniometer is then positioned at the synchrotron facility such that this crystallographic direction is orientated parallel to the direction of polarization of the synchrotron X-ray beam. This polarization vector (this is a vector in crystal Cartesian base of the single crystal sample) calculated as [0.81 0.54 –0.24] in crystal Cartesian base was then applied to FEFF calculations to account for the polarization effects of the synchrotron beam on the EXAFS signal. Table 9 gives the backscattering paths calculated for M1 and M2 site in this synthetic Th-doped FAP with the polarization vector [0.81 0.54 –0.24] applied. Comparing the backscattering paths calculated for M1 and M2 sites with (Table 9) and without (Table 6) applying the polarization vector, we see no major differences such as the absence of paths but rather only the differences in path amplitudes calculated by FEFF.

The experimental data were first fit using the initial parameters calculated for each of the two M sites without applying the polarization correction (Table 6), and by fixing the coordination numbers of shells larger than those of the first nearest neighbor atoms. The raw and fitted k^3-weighted χ functions for the Th-doped synthetic FAP are shown in Figure 5a. The corresponding radial structure functions (RSFs), obtained by Fourier-transformation of the χ functions, are shown in Figure 5b. The data and fit ranges,

TABLE 8. Fitting parameters including fit range (ΔR); data range (Δk); number of independent points in the fit (N_{idp}); number of variables determined in the fit (N_{var}); reduced-chi-square (χ^2_r), and residual (R%)

Sample	ΔR (Å)	Δk (Å^{-1})	N_{idp}	N_{var}	χ^2_r	R%
ThO_2 standard	(1.7–5.7)	(1.1–15.7)	33	9	4	13.8%
Mineville fluorapatite (powder)	(1.5–4.1)	(1.3–11.7)	18	12	16	11.6%
Synthetic fluorapatite (single crystal with P*)	(1.4–4.1)	(0.3–14.4)	19	15	13.4	6.0%
Synthetic fluorapatite (sinlge crystal without P*)	(1.5–4.1)	(0.3–14.4)	19	15	2	2.9%

* P stands for polarization correction.

along with the goodness-of-fit parameters for this fit are shown in Table 8. All scattering paths used and parameters determined in the fit are listed in Table 7.

Similar to the natural Mineville Th-bearing FAP, the first coordination shell is always best fit with 6.76 ± 0.02 O atoms at ~2.36 Å regardless of the starting model, confirming Th substitutes into the M2 site. This is consistent with our results from single-crystal XRD (Luo et al. 2009). Figure 5b shows that the second RSF peak is at R+ΔR ~3.1–3.2 Å. This peak is best fitted by two P atoms at ~3.17 Å. Although the splitting of the third shell is not as obvious as in the Mineville fluoraptite sample, the best-fit model still indicates that the first small peak of the third shell, which is at R+ΔR ~ 3.5–3.7 Å, is attributed to one P atom at 3.52 Å and two P atoms at 3.72 Å. Also, the second peak of the split third shell, which is at R+ΔR ~ 4.1–4.2 Å, is best fitted by 4.95 ± 0.11 Ca atoms at a distance of 4.02 Å together with another 5.05 ± 0.11 Ca atoms at a distance of 4.10 Å. The overall distribution of the second and the slight splitting of the third shell indicate that the coordination environment of Th in this synthetic FAP is similar to M2 site, with two P atoms at 3.168 ± 0.001 Å (in the starting model, there is one P atom at 3.071 Å and one P atom at 3.246 Å), one P atom at 3.525 ± 0.001 Å, two P atoms at 3.718 ± 0.001 Å, ~4.95 ± 0.11 Ca atoms at 4.101 ± 0.001 Å, and ~5.05 ± 0.01 Ca atoms at 4.017 ± 0.001 Å. The fitting approach using M1 site model failed due to the two M1-Ca1 paths at the distance of ~3.42–3.45 Å in the model (Table 6), which do not fit the experimental data.

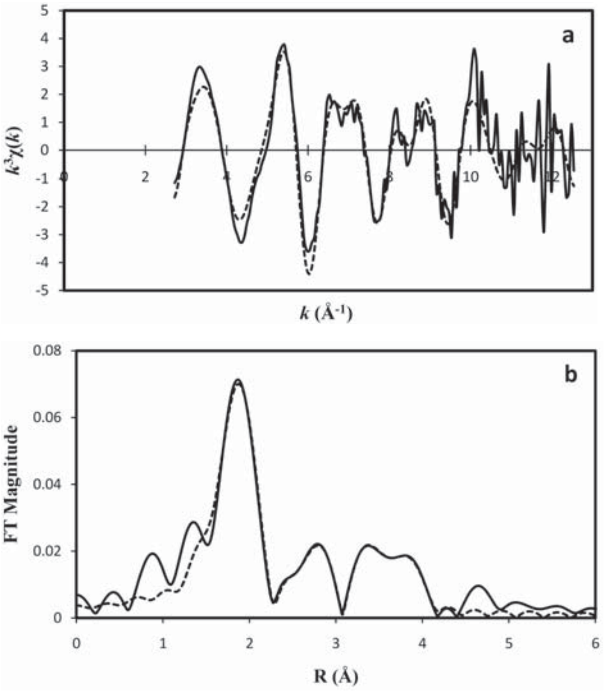

FIGURE 5. EXAFS data and best fits for synthetic fluorapatite without polarization correction. (**a**) The k^3 weighted EXAFS data (solid line) and best fit (dotted line). (**b**) Corresponding Fourier transform amplitudes (solid line) and best fit in R-space (dotted line).

Subsequently, fitting of the experimental data using the initial parameters calculated for each of the two Ca sites after applying the polarization vector (Table 9) was attempted with fixed coordination numbers for shells other than the first. The raw and fitted k^3-weighted χ functions for the Th-doped synthetic FAP are shown in Figure 6a. The corresponding radial structure functions (RSFs), obtained by Fourier-transformation of the χ functions, are shown in Figure 6b. The data and fit ranges, along with the goodness-of-fit parameters for this fit are shown in Table 8. All scattering paths used and parameters determined in the fit are listed in Table 7.

TABLE 9. Coordination environment of M1 and M2 site in oriented single-crystal FAP with vector [0.81 0.54 –0.24] parallel to polarization direction of synchrotron X-ray beam

M1 site				M2 site			
Shell	CN	Amp.	R (Å)	Shell	CN	Amp.	R (Å)
M1-O1	1	100.00	2.369	M2-F	1	100.00	2.288
M1-O1	1	80.89	2.369	M2-O3	1	22.22	2.350
M1-O1	1	89.14	2.369	M2-O3	1	34.87	2.350
M1-O2	1	45.89	2.454	M2-O2	1	76.93	2.383
M1-O2	1	100.00	2.454	M2-O3	1	18.96	2.494
M1-O2	1	43.13	2.454	M2-O3	1	20.68	2.494
M1-O3	1	76.30	2.806	M2-O1	1	17.22	2.683
M1-O3	1	49.70	2.806	M2-P	1	12.60	3.071
M1-O3	1	31.09	2.806	M2-P	1	12.83	3.246
M1-P	1	42.30	3.205	M2-P	1	31.75	3.504
M1-P	1	40.61	3.205	M2-P	1	7.17	3.686
M1-P	1	26.67	3.205	M2-P	1	13.59	3.686
M1-Ca1	1	17.70	3.427	M2-Ca1	1	13.82	3.961
M1-Ca1	1	17.24	3.456	M2-Ca1	1	9.56	3.961
M1-P	1	32.40	3.576	M2-Ca2	1	20.50	3.963
M1-P	1	26.45	3.576	M2-Ca2	1	17.71	3.963
M1-P	1	20.24	3.576	M2-Ca1	1	14.53	4.051
M1-Ca2	1	38.34	3.961	M2-Ca1	1	10.12	4.051
M1-Ca2	1	11.01	3.961	M2-Ca2	1	5.16	4.133
M1-Ca2	1	15.54	3.961	M2-Ca2	1	5.35	4.133
M1-Ca2	1	34.69	4.051	M2-Ca2	1	8.10	4.133
M1-Ca2	1	9.40	4.051	M2-Ca2	1	9.40	4.133
M1-Ca2	1	16.45	4.051				

Similar to fitting results of the data without the polarization correction, the first coordination shell is always best fit with 7.16 ± 0.02 O atoms at ~2.38 Å when using the polarization correction. Figure 6b shows that the second RSF peak is at R+ΔR ~3.1–3.2 Å. The second RSF peak is best fitted by two P atoms at ~3.22 Å. The best-fit model still attributes the first small peak of the third shell at R + ΔR ~3.5–3.7 Å to one P atom at 3.52 Å and two P atoms at 3.73 Å. The second peak of the split third shell, which is at R+ΔR ~4.1–4.2 Å, is best fitted by ~5 Ca atoms at a distance of 3.78 Å together with another ~5 Ca atoms at a distance of 4.14 Å. The overall distribution of the second and the slight splitting of the third shell indicates that the coordination environment of Th in this synthetic FAP single crystal is similar to M2 site, with two P atoms at 3.219 ± 0.002 Å (in the starting model, there are one P atom at 3.071 Å and one P atom at 3.246 Å), one P atom at 3.524 ± 0.009 Å, two P atoms at 3.734 ± 0.007 Å, 4.986 ± 0.820 Ca atoms at 3.778 ± 0.008 Å, and 5.014 ± 0.820 Ca atoms at 4.136 ± 0.004 Å. The fitting approach using M1 site model failed due to the two M1-Ca1 paths at the distance of ~3.42–3.45 Å in the model (Table 6), which could not fit into the experimental data.

The fitting results of EXAFS data from synthetic Th-doped single-crystal FAP with and without applying the polarization correction are similar. Experimental studies show that orientation can have strong effects on micro-EXAFS of single crystal (Brown et al. 1977; Waychunas and Brown 1990; Hudson et

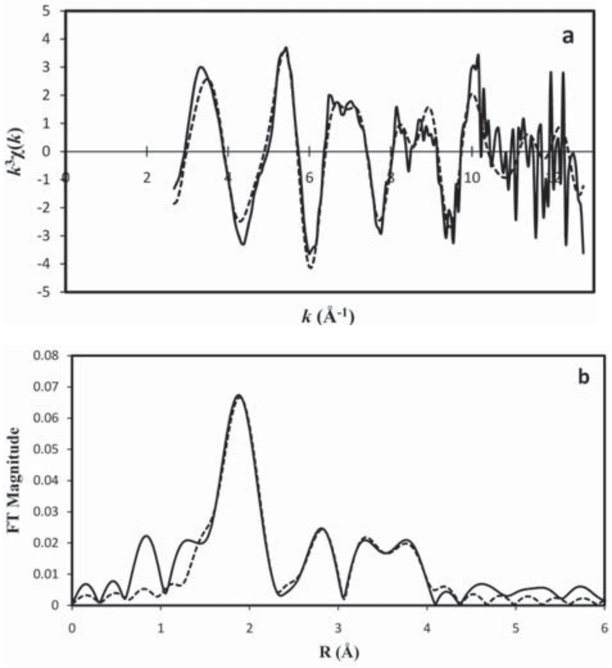

FIGURE 6. EXAFS data and best fits for synthetic fluorapatite after polarization correction. (**a**) the k^3 weighted EXAFS data (solid line) and best fit (dotted line). (**b**) Corresponding Fourier transform amplitude (solid line) and best fit in R-space (dotted line).

al. 1996; Luo et al. manuscript in prep). We speculate that the reason we can fit the micro-EXAFS well, without applying the polarization correction, is that in the specific orientation of synthetic Th-doped single-crystal FAP the models with and without applying polarization correction are very similar to each other. In other words, the polarization effects are minimized at this specific orientation at which data were collected.

DISCUSSION

On the basis of the chemical analysis of both the Mineville FAP and Th-doped synthetic FAP, substitution of Th in FAP is principally compensated by the following mechanisms

$Th^{4+} + 2Na^{+} = 3Ca^{2+}$
$Th^{4+} + 2Si^{4+} = Ca^{2+} + 2P^{5+}$
$Th^{4+} + \square = 2Ca^{2+}$

Radius constraints

The effective ionic radius for nine-coordinated Ca is 1.18 Å, and 1.06 Å in seven-coordination (Shannon 1976). For Th, the ionic radius is 1.09 and ~1.03 Å in nine- and seven-coordination, respectively. Thus for the same stereochemical environment, Th^{4+} is smaller than Ca^{2+}. As discussed earlier, the size of the nine-coordinated M1 site is larger than seven-coordinated M2 site. According to Elliott (1994), this difference in size suggests that ions larger than Ca should favor M1 site, whereas M2 site should be occupied preferentially by ions smaller than Ca. Results from both single-crystal structure refinements and model fits to EXAFS data in this study show that Th substitutes into M2 site in FAP in agreement with this size argument. However, the study by Luo et al. (2009) indicates that U^{4+} and Th^{4+} substitute into M2 site in FAP but into both M1 and M2 sites in chlorapatite (ClAP). Fleet and Pan (1995) pointed out that the effective size of M1 site may be <M2 site because the coordination of M1 site is really 6 + 3 instead of 9. The six closest O atoms constrain the effective size of M1 site in terms of spatial accommodation. Furthermore, Luo et al. (2009) pointed out the preference of U and Th for both M1 and M2 sites in ClAP may be attributable to the large increase in size and distortion of the M2 site upon substitution of Cl for F. This discussion emphasizes the difficulty of estimating site preference of Th in apatite structure by radius constraints alone. To thoroughly understand the site preference of Th in FAP, other important crystal chemical parameters should be considered such as bond valence, substitution mechanisms, and structure variations.

Bond valence

Bond-valence calculations estimate the strength of each cation-anion bond in valence units (v.u.). The calculation of bond valence also provides a bond valence sum, and allows comparison of the formal valence of an ion and its valence in a particular crystal field. The calculation of bond valence has been a powerful first-approximation tool for deducing REE site preference in various studies of apatite structures. According to Fleet and Pan (1995), the M2 site in end-member FAP (Hughes et al. 1989) is underbonded with a bond valence sum of 1.878, whereas the M1 site is slightly overbonded with bond valence sum of 2.016. Therefore, tetravalent Th should prefer M2 site rather than M1 site to increase the bond valence of M2 site. Based on results from single-crystal structure refinements, Luo et al. (2009) pointed out that bond valence for Th^{4+} is 3.53 for M1 site and 3.40 for M2 site in Th-doped single-crystal FAP. This indicates that Th is less underbonded in the M1 site than in the M2 site, based on which Th should favor M1 site over M2 site. However, the estimation by Luo et al. (2009) is based on bond distances of structural sites that are occupied by both Ca (the dominant occupant) and Th, which causes ambiguity in interpretation. We suggest that the bond valence requirements for the single occupied structural site without effects of structural variation should play an important role on the site preference of Th in FAP, in concert with our results showing Th prefers M2 sites in Mineville FAP and synthetic Th-doped FAP. X-ray absorption spectroscopy is element specific, thus in our experiments it probes the local structure around Th only. Calculation of the bond valence for Th^{4+} in M2 site based on bond distances from EXAFS fitting results, yielded bond valence sum of 4.02 for synthetic FAP and 3.70 for Mineville FAP. This suggests the local structure distortion of M2 site upon substitution of Th yields a Th bond valence in M2 site closer to its formal valence state.

Structural accommodation

Fluorapatite has $P6_3/m$ symmetry. Similar to Terra et al. (2009), we can rewrite its unit-cell formula as $Ca1_4Ca2_6(PO1O2O3_2)_6F_2$ according to the different positions that Ca and O atoms occupy in the structure. Figures 3b and 3c show the nearest-neighbor environments of the two Ca sites in FAP. M1 is coordinated to nine O atoms (3×O1 1/2 unit cell below M1, 3×O2 1/2 unit cell above M1, 3×O3 coordinated through to the prism faces formed by the six coordinating O1 + O2 atoms) in a tricapped trigonal prism—$M1O1_3O2_3O3_3$. M2 bonds to six O atoms (1×

O1, 1×O2, and 4×O3) and one column anion (F in this case of FAP), that forms an irregular polyhedron with a hemisphere of six O atoms capped by an F atom—M2O1O2O3$_4$F. These two Ca polyhedra are hexagonally disposed about a central [001] hexad. More specifically, M1 shares O atoms with phosphate tetrahedra and forms an M1-PO$_4$ ring-like framework; M2 sites form triangles centered on F atom, which lie perpendicular to c-axis, and can be thought of as part of the F anion channel in FAP structure (Fig. 3a).

The mean M2-O bond distance in Th-free natural FAP (Hughes et al. 1989) is ~2.44 Å. Upon substitution of Th in the M2 site in the synthetic FAP sample, EXAFS fitting results with and without polarization vector both indicate an average Th-O distance of ~2.36 Å; a difference of 0.08 Å. According to (Shannon 1976), the effective ionic radii for Ca and Th in sevenfold coordination are 1.06 and ~1.03 Å, respectively. This difference of 0.03 Å between the Ca and Th radii in sevenfold coordination of the M2 site alone cannot account for the decrease of ~0.08 Å average bond distance around the M2 site upon Th substitution. This suggests that there must be local structure distortion associated with the shrinkage of M2 polyhedron. There are seven apex points of the M2 polyhedron, four points are connected to four PO$_4$ polyhedra through corner sharing one O atom (one O1, one O2, two O3), two points are connected to one PO$_4$ polyhedra through edge sharing two O3 atoms, and one apex is the F anion (Fig. 3c). Comparing the M2 site in Th-free FAP model (Table 6) with the M2 site in Th-doped synthetic FAP (Table 7), we found that the mean M2-P (second shell) distance increases from ~3.44 to ~3.46 Å and the mean M2-Ca (third shell) distance stays the same at 4.06 Å upon substitution of Th. This suggests the local structure distortion around M2 site to accommodate smaller Th^{4+} extends past the first nearest neighbor coordination shell (M2-O) to the second nearest neighbor coordination shell (M2-P) and does not affect the third nearest neighbor coordination shell (M2-Ca). We suggest the substitution of Th in the M2 site causes an overall shrinkage of the M2 polyhedron and potentially rotations of the PO$_4$ polyhedra that are linked with M2 site, which results in longer M2-P distances. The M2 site is the only Ca position coordinated to the F anion, which forms the anion F channel in the M1-PO$_4$ framework. Several studies suggest the M2 site is a fairly open site and readily accommodates substituents to minimize volume strain without disrupting the M1-PO$_4$ framework in FAP and OHAP (Pan and Fleet 2002; Tang et al. 2009). We speculate that the preference of M2 site over M1 site of Th in this synthetic FAP is to avoid disrupting M1-PO$_4$ framework. However, Rakovan et al. (2002) suggests that U^{6+} prefers the M1 site in FAP and its substitution causes a potential rotation of the distorted M1 trigonal prism, whereas Luo et al. (2009) observed U^{4+} substitutes in the M2 site in FAP. Further studies on factors such as charge compensation mechanism and substitution mechanism of U^{4+} in FAP are required to explain this discrepancy.

EXAFS fitting results of Th-bearing Mineville FAP give the average M2-O bond distance of ~2.39 Å, which also indicates a decrease of ~0.05 Å average bond distance around the M2 site compared to Th-free natural FAP (Hughes et al. 1989). However, the fitting results show that the average M2-P distance in Mineville FAP decreases slightly, which is different from the results of Th-doped synthetic FAP that suggest a increase of M2-P average distances. We suggest that the differences in the EXAFS results from Mineville FAP and synthetic Th-doped FAP are attributable to the presence of REE in Mineville FAP. As indicated by chemical analysis of Mineville FAP (Tables 1–2), there are large amounts of REE such as La, Ce, and Nd in Mineville FAP. Studies by Hughes et al. (1991) and Fleet and Pan (1995) pointed out that La, Ce, and Nd favor the M2 site in FAP based on bond-valence calculations and single-crystal structure refinements. Thus the coexistence of the REE with Th in M2 site may cause the slightly different effects on the structural distortion of M2 site in Mineville FAP than in synthetic Th-doped FAP. However, estimation of the effects of individual REE on the structural distortion of M2 site is hampered by the inability of the conventional diffraction methods to distinguish among individual elements on multiply occupied sites.

ACKNOWLEDGMENTS

This work was supported by NSF grant EAR-0409435 (J.R. and J.M.H.) and EAR-0003201 (J.M.H. and J.R.). Y.T. acknowledges support by S.T. Martin at Harvard University. We thank Syed Khalid at X18B and James Ablett at beamline X27A, NSLS and Matt Newville and Steve Sutton at sector 13, APS for their help for setting up our EXAFS experiments. William Lack and Barry Landrum of the Miami Instrumentation Laboratory are gratefully acknowledged for maintaining the X-ray instrumentation and building our experimental goniometer used for EXAFS data collection.

REFERENCES CITED

Altschuler, Z.S., Clarke, R.S., Jr., and Young, E.J. (1958) Geochemistry of uranium in apatite and phosphorite. Geological Survey Professional Paper, 314-D, 45–90.

Ankudinov, A.L. and Rehr, J.J. (1997) Relativistic calculations of spin-dependent X-ray-absorption spectra. Physical Review B, 4, 1712–1715.

Bostick, W.D., Jarabek, R.J., Bostick, D.A., and Conca, J.L. (1999) Phosphate-induced metal stabilization: Use of apatite and bone char for the removal of soluble radionuclides in authentic and simulated DOE groundwater. Advances in Environmental Research, 3, 488–498.

Bros, R., Carpena, J., Sere, V., and Beltritti, A. (1996) Occurrence of Pu and fissiogenic REE in hydrothermal apatites from the fossil nuclear reactor 16 at Oklo (Gabon). Radiochimica Acta, 78, 277–282.

Brown, G.S., Eisenberger, P., and Schmidt, P. (1977) Extended X-ray absorption fine structure studies of oriented single crystals. Solid State Communications, 2, 201–203.

Bruker (1997) SADABS, SAINT, SMART, and SHELXTL. Bruker AXS Inc., Madison, Wisconsin.

Carpena, J. and Lacout, J.L. (1998) Process for the conditioning of radioactive waste using phosphosilicated apatites as the confinement matrix. U.S. Patent 5771472. U.S. Patent and Trademark Office, Alexandria, Virginia.

Carpena, J., Boyer, L., and Lacout, J.L. (2003) Method to confine plutonium in apatitic ceramics and products obtained using said process. U.S. Patent 6624339. U.S. Patent and Trademark Office, Alexandria, Virginia.

Cary, H. and Helzer S. (2005) Modern Welding Technology, Prentice Hall, New Jersey.

Chen, X., Wright, J.V., Conca, J.L., and Peurrung, L.M. (1997a) Effects of pH on heavy metal sorption on mineral apatite. Environmental Science and Technology, 3, 624–631.

——— (1997b) Evaluation of heavy metal remediation using mineral apatite. Water Air and Soil Pollution, 1–2, 57–78.

Conca, J.L. and Wright, J. (2006) An apatite II permeable reactive barrier to remediate groundwater containing Zn, Pb, and Cd. Applied Geochemistry, 21, 1288–1300.

Elliott, J.C. (1994) Structure and Chemistry of the Apatites and Other Calcium Orthophosphates, 387 p. Elsevier, New York.

Ewing, R.C. and Wang, L. (2002) Phosphates as nuclear waste forms. In M.J. Kohn, J. Rakovan, and J.M. Hughes, Eds., Phosphates—Geochemical, geobiological, and materials importance, vol. 48, p. 673–699. Reviews in Mineralogy and Geochemistry, Mineralogical Society of America, Chantilly, Virginia.

Farley, K.A. and Stockli, D.F. (2002) (U-Th)/He dating of phosphates: Apatite, monazite, and xenotime. In M.J. Kohn, J. Rakovan, and J.M. Hughes, Eds., Phosphates—Geochemical, geobiological, and materials importance, vol. 48, p. 559–577. Reviews in Mineralogy and Geochemistry, Mineralogical Society of America, Chantilly, Virginia.

Fleet, M.E. and Pan, Y. (1995) Site preference of rare earth elements in fluorapatite. American Mineralogist, 80, 329–335.

Foose, M.P. and McLelland, J.M. (1995) Proterozoic low-Ti iron-oxide deposits in New York and New Jersey: relation to Fe-oxide (Cu-U-Au-rare element) deposits and tectonic implications. Geology, 23, 665–668.

Harrison, T.M., Catlos, E.J., and Montel, J.M. (2002) U-Th-Pb dating of phosphate minerals. In M.J. Kohn, J. Rakovan, and J.M. Hughes, Eds., Phosphates—Geochemical, geobiological, and materials importance, vol. 48, p. 523–558. Reviews in Mineralogy and Geochemistry, Mineralogical Society of America, Chantilly, Virginia.

Hudson, E.A., Allen, P.G., Terminello, L.J., Denecke, M.A., and Reich, T. (1996) Polarized X-ray-absorption spectroscopy of the uranyl ion: Comparison of experiment and theory. Physical Review B, 1, 156.

Hughes, J.M. and Rakovan, J. (2002) The crystal structure of apatite, $Ca_5(PO_4)_3(F,OH,CL)$. In M.J. Kohn, J. Rakovan, and J.M. Hughes, Eds., Phosphates—Geochemical, geobiological, and materials importance, 48, p. 13–49. Reviews in Mineralogy and Geochemistry, Mineralogical Society of America, Chantilly, Virginia.

Hughes, J.M., Cameron, M., and Crowley, K.D. (1989) Structural variations in natural F, OH, and Cl apatites. American Mineralogist, 74, 870–876.

Hughes, J.M., Cameron, M., and Mariano, A.N. (1991) Rare-earth-element ordering and structural variations in natural rare-earth-bearing apatites. American Mineralogist, 76, 1165–1173.

Kelly, S.D., Hesterberg, D., and Ravel, B. (2008) Analysis of soils and minerals using X-ray absorption spectroscopy. In A.L. Ulery and L.R. Drees, Eds., Methods of soil analysis, p. 367. Soil Science Society of America, Madison, Wisconsin.

Knox, A.S., Adriano, D.C., Hinton, T.G., Kaplan, D.I., and Wilson, M.D. (2003) Apatite and phillipsite as sequestering agents for metals and radionuclides. Journal of Environmental Quality, 2, 515–525.

Krauskopf, K.B. (1986) Thorium and rare-earth metals as analogs for actinide elements. Chemical Geology, 55, 323–335.

Larsen Jr., E.S., Harrison, H.C., and Keevil, N.B. (1952) Method for determining the age of igneous rocks using the accessory minerals. Geological Society of America Bulletin, 63, 1045–1052.

Lung, M. and Gremm, O. (1998) Perspectives of the thorium fuel cycle. Nuclear Engineering and Design, 2, 133–146.

Luo, Y., Hughes, J.M., Rakovan, J., and Pan, Y.M. (2009) Site preference of U and Th in Cl, F, and Sr apatites. American Mineralogist, 94, 345–351.

Lupulescu, M.V. (2003) Kiruna-type iron deposits in the Adirondack Mountains: Mineville, Essex Co., New York. Geological Society of America Annual Meeting, Seattle, Washington, November 2003. Abstracts with programs, 35, 231.

Lupulescu, M.V. and Pyle, J.M. (2006) The Fe-P-REE deposit at Mineville, Essex Co., New York: Manifestations of Precambrian and Mesozoic fluid infiltration events. Geological Society of America Annual Meeting, Saratoga Springs, New York, March 2005. Abstracts with programs, 37, 4.

McKeown, F.A. and Klemic, H. (1954) Rare-earth-bearing apatite at Mineville, Essex County, New York. Geological Survey Bulletin, 1046-B, 9–23.

McLelland, J.M., Chiarenzelli, J., Isachsen, Y., and Whitney, P. (1988) U-Pb zircon geochronology of the Adirondack Mountains and implications for their geologic evolution. Geology, 16, 920–924.

Meis, C., Gale, J.D., Boyer, L., Carpena, J., and Gosset, D. (2000) Theoretical study of Pu and Cs incorporation in a mono-silicate neodymium fluorapatite $Ca_9Nd(SiO_4)\ (PO_4)_5F_2$. Journal of Physical Chemistry A, 104, 5380–5387.

Newville, M. (2001) IFEFFIT: Interactive XAFS analysis and FEFF fitting. Journal of Synchrotron Radiation, 8, 322–324.

Oosthuyzen, E.J. and Burger, A.J. (1973) The suitability of apatite as an age indicator by the uranium-lead isotope method. Earth and Planetary Science Letters, 18, 29–36.

Pan, Y. and Fleet, M.E. (2002) Compositions of the apatite group minerals: substitution mechanisms and controlling factors. In M.J. Kohn, J. Rakovan, and J.M. Hughes, Eds., Phosphates—Geochemical, geobiological, and materials importance, vol. 48, p. 13–49. Reviews in Mineralogy and Geochemistry, Mineralogical Society of America, Chantilly, Virginia.

Pasero, M., Kampf, A.R., Ferraris, C., Pekov, I.V., Rakovan, J., and White, T. (2010) Nomenclature of apatite supergroup minerals. European Journal of Mineralogy, 22, 163–179.

Patnaik, P. (2003) Handbook of Inorganic Chemicals, 931 p. McGraw-Hill, New York.

Raicevic, S., Wright, J.V., Veljkovic, V., and Conca, J.L. (2006) Theoretical stability assessment of uranyl phosphates and apatites: Selection of amendments for in situ remediation of uranium. Science of the Total Environment, 355, 13–24.

Rakovan, J. and Hughes, J.M. (2000) Strontium in the apatite structure: Strontian fluorapatite and belovite-(Ce). Canadian Mineralogist, 38, 839–845.

Rakovan, J., Reeder, R.J., Elzinga, E.J., Cherniak, D., Tait, C.D., and Morris, D.E. (2002) Characterization of U(VI) in the apatite structure by X-ray absorption spectroscopy. Environmental Science and Technology, 36, 3114–3117.

Ressler, T. (1997) WinXAS: A new software package not only for the analysis of energy-dispersive XAS data. Journal de Physique IV, 7, 269–270.

Shannon, R.D. (1976) Revised effective ionic radii and systematic studies of interatomic distances in halides and chalcogenides. Acta Crystallographica, A32, 751–761.

Soulet, S., Chaumont, J., Krupa, J.C., Carpena, J., and Ruault, M.O. (2001) Determination of the defect creation mechanism in fluoroapatite. Journal of Nuclear Materials, 289, 194–198.

Tang, Y., Chappell, H.F., Dove, M.T., Reeder, R.J., and Lee, Y.J. (2009) Zinc incorporation into hydroxylapatite. Biomaterials, 30, 2864–2872.

Terra, J., Dourado, E.R., Eon, J.G., Ellis, D.E., Gonzalez, G., and Rossi, A.M. (2009) The structure of strontium-doped hydroxyapatite: An experimental and theoretical study. Physical Chemistry Chemical Physics, 11, 568–577.

Terra, O., Dacheux, N., Audubert, F., and Podor, R. (2006) Immobilization of tetravalent actinides in phosphate ceramics. Journal of Nuclear Materials, 352, 224–232.

Trocellier, P., Haddi, A., Poissonnet, S., Bonnaillie, P., and Serruys, Y. (2006) Thorium and cerium chemical behavior in ion-irradiated alkali-borosilicate glasses. Nuclear Instruments and Methods in Physics Research B, 249, 145–149.

Waychunas, G.A. and Brown, G.E. (1990) Polarized X-ray absorption spectroscopy of metal ions in minerals—Applications to site geometry and electronic structure determination. Physics and Chemistry of Minerals, 17, 420–430.

Weber, W.J., Ewing, R.C., and Meldrum, A. (1997) The kinetics of alpha-decay-induced amorphization in zircon and apatite containing weapons-grade plutonium or other actinides. Journal of Nuclear Materials, 250, 147–155.

Wright, J.V. and Conca, J.L. (2004) Using PIMS with apatite II to remediate U and Pu in the environment. Abstracts of Papers of the American Chemical Society, 227, U89.

Manuscript received October 30, 2009
Manuscript accepted June 7, 2010
Manuscript handled by Lars Ehm